Research Square

Preprints are preliminary reports that have not undergone peer review.
They should not be considered conclusive, used to inform clinical practice,
or referenced by the media as validated information.

A physiology-anchored, full-channel whole-worm platform: building Caenorhabditis elegans in silico, block by block, from measured constants

Huan Li

HL@liangtabio.com

Shanghai Liangta Biotech Co., Ltd. https://orcid.org/0009-0004-2695-6825

Research Article

Keywords: C. elegans, connectome, conductance-based model, neuromuscular junction, proprioception, neuropeptide, parameter provenance, computational neuroethology

Posted Date: November 11th, 2026

DOI: https://doi.org/10.21203/rs.3.rs-11389227/v2

License: This work is licensed under a Creative Commons Attribution 4.0 International License.
Read Full License

Additional Declarations: The authors declare no competing interests.

A physiology-anchored, full-channel whole-worm platform: building *Caenorhabditis elegans* in silico, block by block, from measured constants

Huan Li
Shanghai LiangTa biotech Co., Ltd.
hl@liangtabio.com
ORCID: 0009-0004-2695-6825

October 2026

Abstract

Understanding how a nervous system generates behaviour requires knowing whether the biology already measured is sufficient to explain it. Whole-animal simulators of *C. elegans* have so far answered by *fitting*: synaptic weights, channel densities, or reduced oscillator units are trained until the output looks biological — which shows that the fitter works, not that the biology is understood. Here we take the opposite route: we assemble a whole-animal model of *C. elegans* entirely from published experimental measurements and ask how much behaviour the literature alone can produce. Every one of the 323 connectome cells (283 neurons, 7 glial cells, 32 head muscle cells, 1 remnant; 4,450 chemical and 1,219 gap-junction edges weighted by electron-microscopy contact counts) integrates 17 ionic currents whose gating constants are anchored to voltage-clamp electrophysiology, extracted with a pipeline inherited from our cardiac channel work; a newly built 96-cell body-wall muscle layer and a 24-segment viscoelastic body close the loop through measured proprioceptive coupling. No parameter is trained (Tables 4, 5). Without fitting anything, the frozen platform quantitatively reproduces the animal's core behavioural repertoire: forward crawling at 0.222 vs. 0.21 mm s^{-1} and 0.62 vs. 0.58 Hz, steady backward locomotion, salt chemotaxis through both known strategies (final approach +3.46 mm), touch- and ASH-triggered escape reversals, command-state switching, and RIS-driven arrest. Three biological results fall out. First, locomotor information does not broadcast from a central pattern generator: it travels as a proprioception-coupled stadium wave through the motor-neuron chain and the muscle rows ($\lambda \approx 10$ segments at 0.62 Hz). Second, the platform validates mechanistically: removing the TRP-4 stretch-feedback arm reproduces the exaggerated-bending phenotype of *trp-4(lf)* animals, and reinstating the arm rescues wild-type curvature. Third, it exposes a discovery: the strongest extrasynaptic functional edge in the whole-animal signal-propagation atlas originates from a neuron whose two marker peptides have no recorded receptor, yielding a falsifiable ligand–receptor prediction. The remaining gaps (ASH gain modulation, a residual crawl bias, the 90 unimplemented neuropeptide systems) are reported with the same bookkeeping. Because every constant is sourced, each future experimental result enters the platform as a module, not a re-fit — turning half a century of *C. elegans* measurement into a living, testable whole-animal model.

Keywords: *C. elegans*; connectome; conductance-based model; neuromuscular junction; proprioception; neuropeptide; parameter provenance; computational neuroethology

1 Introduction

This project began with a simple frustration: in whole-animal modelling, the answer can be manufactured. If a simulator reproduces worm locomotion after its weights were trained on worm locomotion, the result tells us the fitting worked — not that the anatomy is understood. The same objection applies to channel-level models whose conductances are fitted to target activity, and to reduced models whose oscillator units are distilled from recorded kinematics. What would happen instead if every number in a whole-animal model were required to carry a citation?

Two earlier lines of work made the attempt feasible. First, the anatomy is now essentially complete: synaptic-resolution connectomes of both sexes [2, 3, 1], the neuropeptidergic "wireless" connectome [15, 16], and

quantitative behavioural reference values from crawling mechanics to chemotaxis strategy [45, 46, 47, 68, 54]. Second, our own cardiac channel programme established an extraction pipeline that treats digitized voltage-clamp traces as measurements rather than fitting targets — chord-conductance activation, anchored reversal potentials, Boltzmann steady states with R^2 quality gates and bootstrap intervals — and showed on four cardiac channels including hERG that such constants yield parameter-efficient predictive models [29]. The same pipeline, run on 338 cell-line recordings across eight channel classes, reproduced every literature spot-check available (Table 3).

Here we port both ingredients into a single whole-animal platform. The design rule is modular: the model is a stack of layers — connectome, excitability, synapses, muscles, body, proprioception, neuromodulation — and each layer is built from the corresponding experimental literature, with the provenance of every constant recorded in an anchor ledger (Tables 4–5). Where the literature is silent we do not invent a number and call it measured: we either derive a bound and declare the estimate, or leave the module out and declare the gap. The result is a frozen, fully observable *C. elegans*: every channel of every cell at every millisecond is accessible, and behaviour is reported against wet-lab references rather than against fitted targets.

We then ask the platform the only question that justifies it: how much of the animal does the literature already explain? The answer, quantified below, is: forward and backward locomotion with realistic kinematics and a travelling proprioceptive wave; salt chemotaxis by both known strategies; touch and chemical escape; command-state switching and RIS arrest; and one mutant phenotype (*trp-4*) reproduced and rescued. What the literature does *not* yet explain is stated just as plainly.

2 Results

2.1 A literature-anchored whole-animal platform

Fig. 1 and Table 1 summarize the stack. The EM connectome contributes 323 cells: 283 neurons, seven glial cells (three GLR and four CEP sheath cells), one reconstruction remnant, and 32 head-region body-wall muscle cells that carry their own channel inventory and gap-junction into the network [2, 3]. The somatic coverage includes every locomotory, steering, touch and chemo/thermosensory class — including the tail sensory classes (PHA, PHB, PHC, PLM, PDE, PQR, PVM, PVW, LUA, URY) absent from earlier releases of this model line; only the pharyngeal network is excluded. Functional composition: 79 sensory neurons (among them the proprioceptive DVA), 80 interneurons (including the ten command cells of classes AVA, AVB, AVD, AVE and PVC), and 121 motor and head-motor neurons; three cells remain of undetermined class (VAn, CANL, CANR). A per-cell classification with sources is provided as Supplementary Table S5. On top of this sits the actuation layer: 96 body-wall muscle cells arranged as 24 rows × 4 quadrants (DL, DR, VL, VR), matching the anatomical muscle map [1].

Every cell is a conductance-based point cell with 29 state variables and 17 ionic current types — 12 K^+ currents (shal, shak, kir, kqt-3, egl-2, egl-36, kvs-1, bk, slo-1, bk2, slo-2, sk), three Ca^{2+} currents (unc-2, cca-1, egl-19), the Na^+ leak channel nca, and a linear leak — plus an intracellular Ca^{2+} pool and Ca^{2+}-dependent gating (Methods). Synapses are graded, with sign from transmitter identity; gap junctions are ohmic with a state-dependent conductance anchored on *unc-1* measurements [38]. Motor output reaches the muscle layer through cholinergic and GABAergic neuromuscular junctions with the measured excitation:inhibition current ratio of 0.61 [43]; muscles integrate excitation through a two-stage cascade (15.5 ms electrical, 300 ms calcium/contraction) anchored to muscle action-potential recordings [42, 41], and are coupled by innexin gap junctions with the measured coupling coefficient 0.25 [44]. Muscle activation sets the preferred curvature of a 24-segment viscoelastic rod whose bending elasticity is taken from biomechanical measurement [45], and segmental curvature feeds back onto B-class motor neurons through the proprioceptive coupling characterized by Wen et al. [7] and onto the stretch receptor DVA/TRP-4 [18]. Two peptidergic axes (DVA→NLP-12→CKR-2 [17]; FLP-14→FRPR-19 [58]) modulate NMJ gain and reversal-bout persistence.

2.2 Channel constants: an extraction pipeline inherited from the cardiac line

The single most consequential design choice is how channel constants enter the model. The gating equations (sigmoid steady states, bell-shaped time constants, Ca^{2+}-nanodomain coupling of BK currents) follow the published single-neuron models of Nicoletti et al. [35, 36], fitted in that work to *C. elegans* voltage-clamp recordings [30, 31, 32, 33, 34]. On top of this adopted base we run our own extraction pipeline — developed and validated on the cardiac line [29] — on digitized public voltage-clamp data (Channelpedia CAEEL collection [37]): chord-conductance activation instead of tail currents where the latter carry capacitive artefacts; reversal

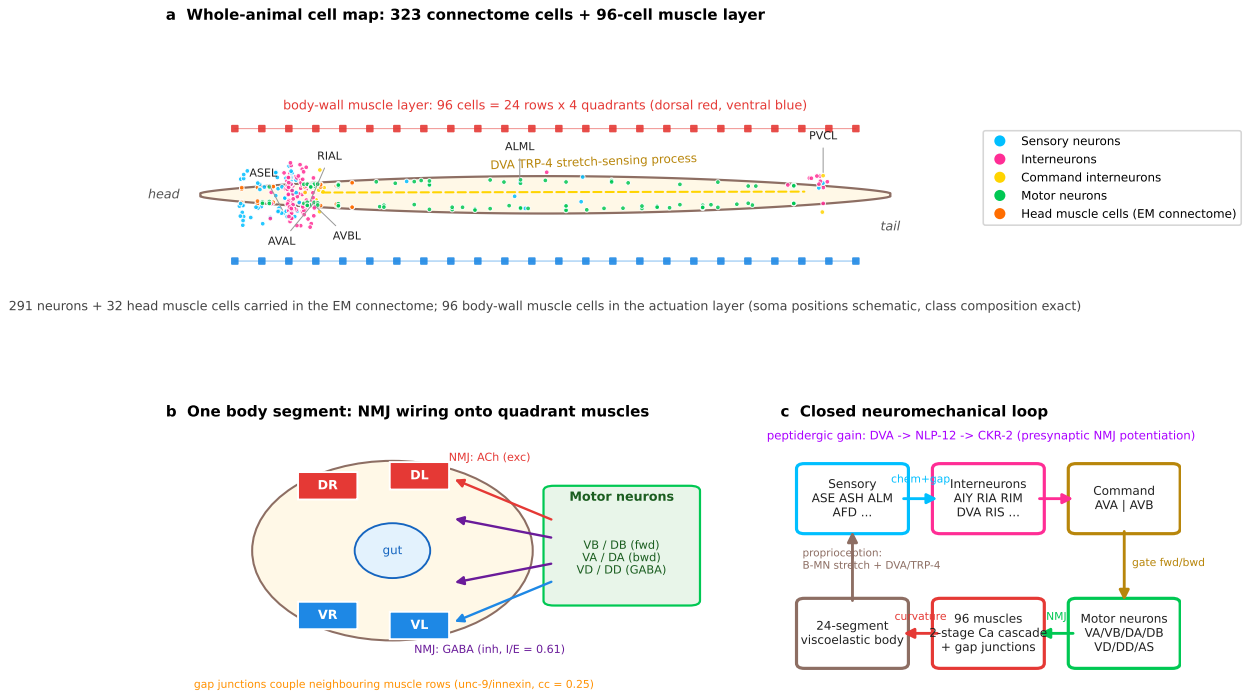


Figure 1. The platform. a, Whole-animal cell map: the 323 EM-connectome cells (dots, coloured by functional class) and the 96-cell body-wall muscle layer (squares: 24 rows × 4 quadrants; dorsal red, ventral blue). Soma positions are schematic along the anterior–posterior axis; class composition is exact. The dashed line marks the stretch-sensing process of DVA (TRP-4) along the ventral cord [18]. **b,** One body segment: motor-neuron classes wire onto quadrant muscles through cholinergic (excitatory) and GABAergic (inhibitory) NMJs with measured current ratio I/E = 0.61 [43]; neighbouring muscle rows are coupled by innexin gap junctions [44]. **c,** The closed loop: sensory→interneuron→command→motor →muscle→body, closed by two proprioceptive paths (B-motor-neuron stretch coupling [7]; DVA/TRP-4 [18]) and one peptidergic gain axis (DVA→NLP-12→CKR-2 [17]).

potentials anchored at the measured I–V zero-crossing; least-squares Boltzmann steady states with R^2 quality gates and bootstrap confidence intervals; delayed single-exponential time constants. Ten channel datasets were re-derived; Table 2 reports the three with publication-grade fits against the adopted constants. Substituting the re-derived sets into the frozen model leaves whole-animal kinematics unchanged (forward speed $\Delta = +0.008\%$), an early instance of the network-level robustness quantified previously [29].

The pipeline's credibility rests on direct measurement discipline: fits are estimators, and every constant carries its QC flags. Run over 338 cell-line recordings across eight mammalian channel classes, the same code reproduced every available literature spot-check (Table 3); that population-level master table is the methodological bridge from the cardiac work to the present worm model.

2.3 Every constant has a source: the anchor ledger

Table 4 lists the constants taken directly from measurements; Table 5 lists constants whose *mechanism* is anchored in the literature but whose *value* is a bounded estimate, with the bound and its sensitivity record; the ledger further records protocol parameters (not model constants) and four historical values that were removed or zeroed once their provenance failed review. Nothing in the running configuration is an unlabelled free knob. The practical consequence: when a behaviour fails, we know which layer is speaking — and when it succeeds, the success is attributable to specific papers.

2.4 Control topology: who talks to whom, in contact numbers

Because weights are EM contact counts, the network's control topology is a measured object, not a design choice. Fig. 3 renders the frozen network as a layered directed graph. The dominant flows are quantitative statements about the animal: the strongest single-class conduits are the interneuron→motor and interneuron→muscle projections, and the sensory layer reaches the command layer both directly (ASH→AVA, ALM→AVD/PVC [22, 57]) and through the AIY/RIA steering axis [53, 55]. Gap junctions add the measured electrical biases,

Table 1. Platform layers, content and provenance.

Layer	Content	Source
Connectome	323 cells (283 neurons, 7 glia, 32 head muscle, 1 remnant); 4,450 chemical + 1,219 gap edges; weights $\propto$ EM contact number; signs from transmitter identity	Cook 2019 [2]; Witvliet 2021 [3]; White 1986 [1]
Neuron dynamics	29 ODEs/cell; 17 currents; anchored + re-derived kinetic constants	Eq. (1); Refs. [35, 36, 30, 31, 32, 33, 34]; Table 2
Synapses	Graded release table (slope 1/25 mV^{-1}, cap 1.5); unit conductance $g_{\mathrm{syn}} = 0.02$ (bounded)	Narayan 2011 [50] (bounded estimate, §2.3)
Gap junctions	Ohmic; state-dependent gain $g_{\mathrm{eff}} = (1 - k(1 - M))\, G_{\mathrm{gap}}\, w$, $k = 0.7$	Chen 2007 [38]; Kawano 2011 [67]
Muscles & NMJ	96 cells, 24×4 quadrants; two-stage cascade 15.5 ms + 300 ms; NMJ I/E = 0.61; muscle GJ cc = 0.25	Gao & Zhen 2011 [42]; Liu 2011 [41, 44]; Liu 2009 [43]
Body	24-segment viscoelastic rod; preferred curvature; bending elasticity $b = 4 \times 10^{-12}$ N m^3	Fang-Yen 2010 [45]; formulation after Boyle & Cohen [5, 6]; equations of motion after Chung [9]; original implementation (this work)
Proprioception	B-motor-neuron stretch coupling ($\tau_c = 80$ ms, span 0.2 L, slope 0.62)	Wen 2012 [7]
Peptidergic	DVA→NLP-12→CKR-2 NMJ gain; FLP-14→FRPR-19 bout feedback	Hu 2011 [17]; Li 2006 [18]; Marques 2021 [58]

Table 2. Re-derived channel constants vs. adopted values. Least-squares Boltzmann fits to digitized CAEEL data [37] (R^2 in parentheses). Adopted values: published single-cell fits [35, 36] used in the frozen model (†converted to gate level, m^3). Substitution into the calibrated model leaves behaviour unchanged (§2.2).

Current	Constant	Re-derived (this work)	Adopted [35, 36]
SHK-1 (shak)	act. $V_{1/2}$, k (mV)	+3.8, 7.18 (0.998)	+20.4, 7.7
	inact. $V_{1/2}$, k (mV)	−18.9, 4.29 (1.00)	−7.0, 5.8
SHL-1 (shal)†	act. $V_{1/2}$, k (mV)	−4.0, 24.6 (0.993)	−6.8, 14.1
	inact. $V_{1/2}$, k (mV)	−35.2, 6.94 (0.999)	−51.1, 8.3
EGL-19	act. $V_{1/2}$, k (mV)	+8.3, 8.34 (1.00)	−4.4, 7.5
	E_{rev} (mV)	+55.1	+60

notably AVB→VB descending drive [62, 67]. This topology is what the behaviours below must — and do — emerge from.

2.5 The muscle layer: 96 cells, measured constants

Earlier releases of this model line used a two-row bang-bang muscle formulation [5]; the present platform replaces it with a 96-cell layer whose every constant is measured (Fig. 4). Each muscle cell integrates its NMJ drive through a first-order electrical stage ($\tau_e = 15.5$ ms, the muscle AP halfwidth [42, 41]) followed by a calcium/contraction stage ($\tau_{Ca} = 300$ ms, the measured neuromuscular delay bound [7], consistent with GCaMP decay [48]); innexin gap junctions between neighbouring rows are solved as a steady-state resistive lattice with coupling 0.25 [44]. The NMJ current ratio I/E = 0.61 comes from paired cholinergic/GABAergic field-stimulation measurements [43], and the muscle electrical constants (rest −26.9 mV, AP amplitude 45.1 mV) come from in-situ patch recordings [41]. Activation maps to preferred curvature $\kappa_0 = \kappa_{\max}(A_D - A_V)$ per segment with $\kappa_{\max} = 16$ mm^{-1} digitized/adjudicated from kinematic data [7, 47]. The muscle layer is the largest single contributor to behavioural realism: replacing the bang-bang layer repaired reversal-wave propagation and removed the head-overbend artefacts of the old actuation (Supplementary Movies).

2.6 Emergent locomotion matches the animal

With a tonic command drive on AVB and no trained parameter, the closed loop self-generates a head-to-tail dorsoventral wave (Fig. 4d, Fig. 6a,b; Supplementary Movie S1). Measured against the animal: forward speed 0.222 mm s^{-1} (real 0.21 [6, 25]), undulation 0.62 Hz (real 0.58), curvature amplitude 4.03 mm^{-1} inside

Table 3. Pipeline validation on cell-line data (338 cells, 8 channel classes). Population medians [IQR] of QC-passed cells from the master table of the sister channel programme; every literature spot-check matched. *15 °C condition (only quantified condition); **activation faster than the 0.1 ms sampling grid (registered as an upper bound, not a fit).

Channel	$V_{1/2}$ median (mV)	k (mV)	τ_{act} (ms)	Literature check
Kv1.2	−2.0 [−7.7, 6.5]	10.1	1.0 [0.6, 1.9]	∼0 mV, fast ✓
Kv3.1	+17.8 [+13.3, +20.6]	16.6	≤1**	+10 to +20 ✓
Kv4.2	+17.9 [−2.0, +25.5]	22.9	12.4 [1.0, 15.4]	peak-mode, Tier-2
Kv7.2	−17.4 [−22.4, +18.8]	20.2	52.7 [39.3, 74.4]	WT cluster ✓
Kv7.3*	+32.3 [+23.9, +44.3]	24.3	84.5 [65.4, 95.4]	right-shifted ✓
HCN2	−88.0 [−94.4, −74.3]	10.0	—	−90 to −100 ✓
Kir2.4	instantaneous rectifier: I–V table used directly			✓
TASK1	+51.0 [+45.2, +56.0]	11.9	105.3 [85.4, 186.5]	near-leak, I–V table

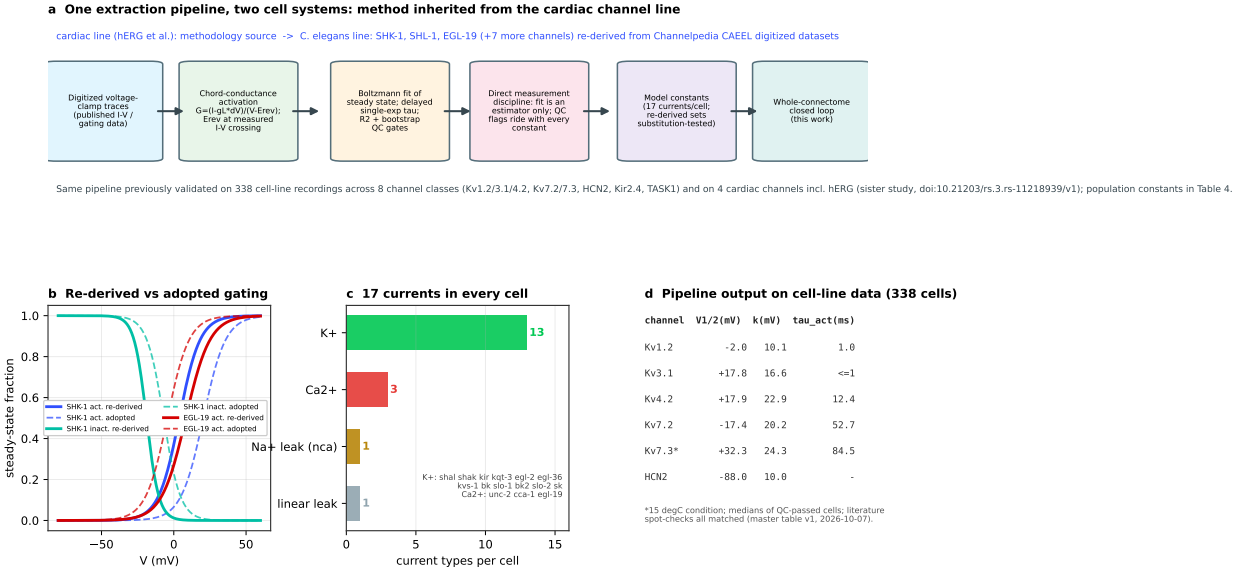


Figure 2. One extraction pipeline, two cell systems. a, The pipeline: digitized voltage-clamp data → chord-conductance activation with anchored E_{rev} → Boltzmann + delayed-exponential fits with R^2/bootstrap QC → model constants. Validated on 338 cell-line recordings and on the cardiac line (hERG et al.) [29]; here applied to *C. elegans* channels (Channelpedia CAEEL [37]). **b,** Re-derived (solid) vs. adopted (dashed) steady-state gating for the three publication-grade re-derivations (Table 2). **c,** The 17-current inventory carried by every cell. **d,** Population medians from the 338-cell master table (Table 3).

the biological band 3–5 mm^{-1} [7, 47], zero backward fraction. Backward locomotion under the reciprocal command state runs at −0.23 mm s^{-1} and 0.47 Hz with bouted structure (median bout 2–3 s, matching [40]) and a tail-to-head wave, as expected from A-class motor-neuron oscillators [63]. The wave is not injected: with the proprioceptive loop opened the same network produces no rhythm, consistent with the proprioception-first view [7, 62, 66].

2.7 The stadium wave: information travels as a proprioception-coupled wave

A central question of this platform is *how* information moves. The answer is visible in Fig. 5: like a stadium wave, the behavioural signal is passed locally from segment to segment rather than broadcast from a central pattern generator. Motor-neuron voltages along the ventral cord show a clean diagonal phase pattern (Fig. 5b); the muscle-activation difference $A_D - A_V$ follows with the mechanical lag documented experimentally [49]; and the phase gradient at the undulation frequency is linear along the body (Fig. 5c), giving $\lambda \approx 10.3$ segments (0.45 body lengths) at $f_0 = 0.62$ Hz, i.e. a wave speed of ≈ 0.28 body lengths per second — the kinematic signature of a travelling wave, produced here by proprioceptive coupling [7, 66] between neighbours rather than by any master oscillator. Panel d shows the instrument side of the same claim: one cell (VB05) is fully observable — voltage, calcium, and the peptidergic state variables riding on top (Supplementary Movie S9).

Table 4. Class A — constants fixed by direct literature measurement.

Constant	Value	Measurement	Source
Proprioceptive slope G_{SR}	0.62	measured slope 0.62 ± 0.03	Wen 2012 [7]
Proprioceptive field span	$0.20\,L$	coupling length $l \approx 200\,\mu$m	Wen 2012 [7]
Coupling delay τ_c	80 ms	$\tau_c = l/v$; max. wave speed $2.6\,\mathrm{mm\,s^{-1}}$	Wen 2012 [7]
Muscle fast tau τ_e	15.5 ms	AP halfwidth 15.5 ± 0.9 ms (∼20 ms)	Gao & Zhen 2011 [42]; Liu 2011 [41]
Muscle slow tau τ_{Ca}	300 ms	neuromuscular delay bound; Ca transient decay (bounded)	Wen 2012 [7]; Butler 2015 [48]
NMJ I/E ratio	0.61	1.23 ± 0.12 vs. 2.01 ± 0.11 nA	Liu 2009 [43]; implemented as 0.60
Muscle gap-junction coupling	cc = 0.25	longitudinal coupling coefficient (unc-9 KO → 0.1)	Liu 2011 JBC [44]
Reversal refractory	4 s	post-reversal response suppression	Wicks & Rankin 1995 [39]
Curvature scale $\kappa_{\max}$	$16\ \mathrm{mm^{-1}}$	digitized curvature range; candidate 10 falsified (speed/chemotaxis anchors break)	Wen 2012 [7]; Broekmans 2016 [47]

Table 5. Class B — mechanism from the literature, value a declared bounded estimate. "Bound/validation" records the sensitivity band or in-model validation on file; none of these values is presented as measured.

Constant	Value	Mechanism anchor	Bound/validation
Gap-junction gain G_{gap}	state-var.	unc-1/innexin state modulation, $k = 0.7$ measured	Chen 2007 [38]; rest $g_{\mathrm{eff}} \approx 0.30$ is arithmetic output
g_{syn} (neuron–neuron)	0.02	AFD→AIY transfer function (only in-vivo neural measurement)	Narayan 2011 [50]; band $[0.01, 0.04]$, in-model gain 1.8× within author bound
SLO negative feedback (sloa, τ, θ)	1.0, 1.0 s, 15 mV	UNC-2→SLO-1/2 activity-dependent K^+ feedback	threshold from measured dV gap; crawl regression bit-identical
A-MN oscillators (amnosc, prop 18, offset 8)	on	A-class motor neurons are local oscillators for backward locomotion	Gao 2018 [63]; band $[12, 70]$ insensitive
AVA bistable plateau (25, 0.5 s)	on	AVA regenerative plateau; UNC-2/EGL-19 plateaus	Meng 2024 [61]; Mellem 2008 [32]; engine voltage scale compressed ∼ 3×, declared
RIS bout terminator (14 pA, 1.0/0.3 s)	on	RIS terminates reversal bouts	Kato 2015 [20]; termination threshold 9–10 pA measured
Peptidergic gains (0.25, 10)	on	NLP-12→CKR-2; FLP-14→FRPR-19	Hu 2011 [17]; Marques 2021 [58]
B-chain proprioception (−12 pA, offset −6)	on	short-range proprioceptive relay	Wen 2012 [7]; sensitivity band on file
Neuron–neuron E:I multiplier	5.0	— (field blank)	**declared estimate**; anatomy checked, no measurement exists
Rectifying gap at AVA	on	electrical bias of backward circuit	Kawano 2011 [67] (concept)
EGL-36 GABA branch gain	0.6	EGL-36 K^+-branch scaling on DD/VD GABAergic motor neurons	declared estimate; crawl regression bit-identical

2.8 Seven behavioural assays against wet-lab references

The frozen platform was run through seven standard assays (Fig. 6, Table 7; Movies S1–S8). Chemotaxis deserves a detailed note because it exercises the two known strategies separately [54, 68]: for moderate heading errors (90°, 270°) the weathervane arm — ASE-reported dC/dt routed through AIY/RIA to the head-steering motor neurons SMD/RIV — curves the animal smoothly onto the source (+3.46 mm final approach for the 90° assay; Fig. 7); for a large 180° error the pirouette arm fires reversal-bout events that re-orient the animal (−111.7° net turn), the Pierce-Shimomura strategy [68]. During development the two arms interfered (the pirouette arm mis-fired on a medium-error assay and destroyed approach); the mechanism-level dissection and repair are documented in Fig. 7 — the sensor was never at fault (ASE statistics identical between the broken and fixed runs), the gating between strategies was. This is the kind of bug only a mechanistic model can localize.

Two assays carry honest caveats. The ASH chemical-escape assay passes only on the second of two pulses: the first pulse fails because the ASH gain modulation layer (INX-20/cGMP/EGL-4 [52]) is not yet built; we score this a weak pass and list it as a gap rather than tune around it. And while backward locomotion is quantitatively realistic, long backward bouts retain a residual J-shaped drift whose root cause (a tail-segment DC-bend bias) is declared in the Limitations.

2.9 Modulatory layers and a mutant phenocopy that falls out for free

Two peptidergic axes are implemented with their published mechanisms: DVA→NLP-12→CKR-2 presynaptic potentiation of cholinergic NMJs [17, 18] and the FLP-14→FRPR-19 positive-feedback arm of reversal bouts [58]; gap-junction conductance is state-dependent following *unc-1* [38]. During a forward→backward switch the two peptide arms activate in their proper behavioural phases (Fig. 8b; Supplementary Movie S10). The

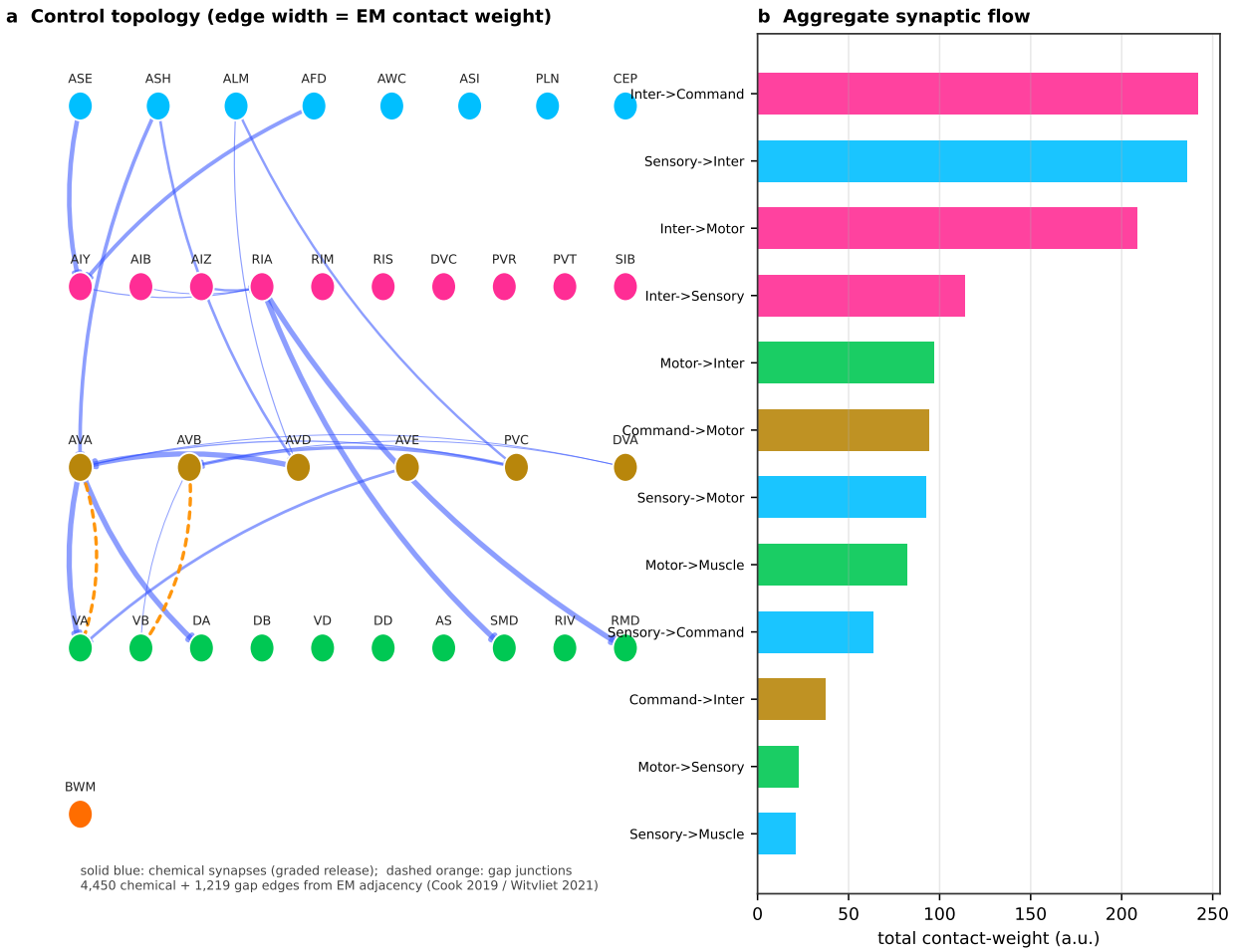


Figure 3. Measured control topology of the frozen network. a, Layered directed graph; edge width encodes aggregated EM contact weight for the principal locomotory and sensory pathways (solid blue: chemical; dashed orange: gap junctions). **b,** Aggregate contact-weight flow between layers (all edges).

strongest validation, however, came from a failure: the AVB-ablated steady-backward configuration showed exaggerated bending ($\kappa_{\text{amp}} \approx 8$ mm^{-1}, 0.105 Hz) — the published phenotype of *trp-4(lf)* mutants [18] — because the TRP-4 negative stretch arm was never part of that configuration. Reinstating the arm rescued wild-type-like curvature ($\kappa_{\text{amp}} \approx 4.3$ mm^{-1}, 0.42 Hz; Fig. 8c). A model that had been built by fitting would have absorbed this defect silently; here it surfaced as a missing module with a name, a phenotype, and a rescue.

3 Discussion

Position among whole-worm models. Table 8 updates the standard comparison. The present platform is, to our knowledge, the only whole-animal *C. elegans* model in which (i) every neuron carries a 17-current conductance-based model with constants anchored to electrophysiology, (ii) synaptic weights come from EM contact counts with zero trained weights, (iii) the muscle layer is itself built from measured NMJ and muscle constants, and (iv) neuromodulatory (peptidergic) layers are simulated dynamically rather than mapped structurally. c302/OpenWorm reaches cell coverage with reduced dynamics and requires an injected pacemaker [11, 12]; worm-whisperer distils the connectome into trained oscillator units [8, 10]; BAAIWorm fits five representative neurons and trains weights on calcium correlations [14]. Our claim is narrower and stronger: with measured anatomy and measured excitability, the behaviours above emerge without any fit to behaviour.

Robustness is inherited, not fitted. In the conductance-only configuration of this model line, single-channel knock-outs that strongly remodel single neurons (resting-potential shifts up to 12 mV, command drive changes up to 47%) changed whole-animal speed and frequency by less than 0.3% in the hERG-line experiments reported previously [29]; the same compensatory structure protects the present platform, in line

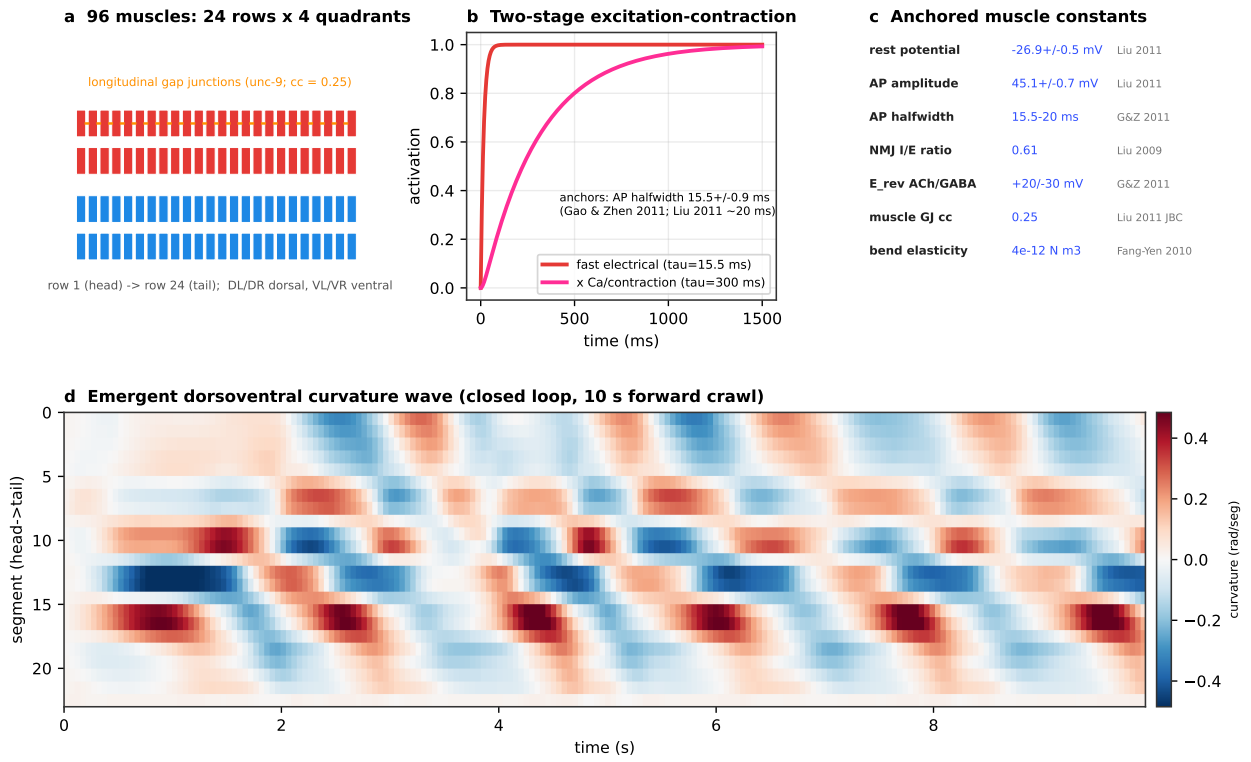


Figure 4. The 96-cell muscle layer and its anchored constants. a, Layout: 24 rows × 4 quadrants; longitudinal innexin gap junctions (cc = 0.25) [44]. **b,** Two-stage excitation–contraction cascade with measured time constants [42, 41, 48]. **c,** Anchored muscle constants (all measured; Table 6). **d,** Emergent dorsoventral curvature wave of the closed loop during 10 s of forward crawling.

Table 6. Muscle-layer constants (all measured). Full constant table with per-row extraction status ships with the model release (`data/muscle96_constants.csv`).

Quantity	Value	Source
Rest potential	-26.9 ± 0.5 mV	Liu 2011 [41]
AP amplitude / halfwidth	45.1 ± 0.7 mV / 15.5–20 ms	Liu 2011 [41]; Gao & Zhen 2011 [42]
E_{rev} ACh / GABA	+20 / −30 mV	Gao & Zhen 2011 [42]
NMJ I/E	0.61 (1.23 vs. 2.01 nA)	Liu 2009 [43]
Muscle GJ coupling (longitudinal)	0.25	Liu 2011 [44]
Bending elasticity b	4×10^{-12} N m^3	Fang-Yen 2010 [45]
Muscle–torque phase (crawl)	$\sim 60°$	Fang-Yen 2010 [45]

with single-cell degeneracy theory [26, 27, 28]. We flag the boundary of this claim: the knock-out panel was quantified on the earlier muscle layer and awaits re-quantification on muscle96.

What the platform cannot yet do (declared, not hidden). (i) ASH chemical escape passes only on the second pulse; the ASH gain-modulation layer (INX-20/cGMP/EGL-4 [52]) is missing. (ii) Forward crawling carries a small leftward drift whose root cause (mapped to a tail-segment DC-bend bias and the RIA head-steering compartments [55]) is the top-priority open defect; it is also the upstream reason the chemotaxis strategy gate must be handled carefully (Fig. 7). (iii) Omega-turn bouts exceed the coil criterion of our own QC; d180 U-turns need two concatenated bouts whereas animals can turn >120° in one [47]. (iv) Neurons are point cells with graded transmission; the engine's voltage scale is compressed by $\sim 3\times$ relative to biological millivolts (declared; all thresholds and plateaus are consistently rescaled). (v) The preferred-curvature body cannot express contracture, so cholinergic drug (aldicarb) end-states are out of scope. (vi) ∼90 neuropeptide systems [15, 16], the monoamine layer, and roaming/dwelling state control are absent; the TRP-4 rescue raises a genuine open question — how the real animal gates this negative arm during omega turns — which we declare rather than paper over. (vii) Whole-brain calcium imaging [20, 19] is not yet used as a constraint; confronting simulated with measured network activity is the sharpest next test.

An actionable gap: the strongest wireless edge runs on an orphan peptide. Item (vi) can be made concrete, and the concretion shows how the ledger principle converts a gap into a falsifiable prediction. The

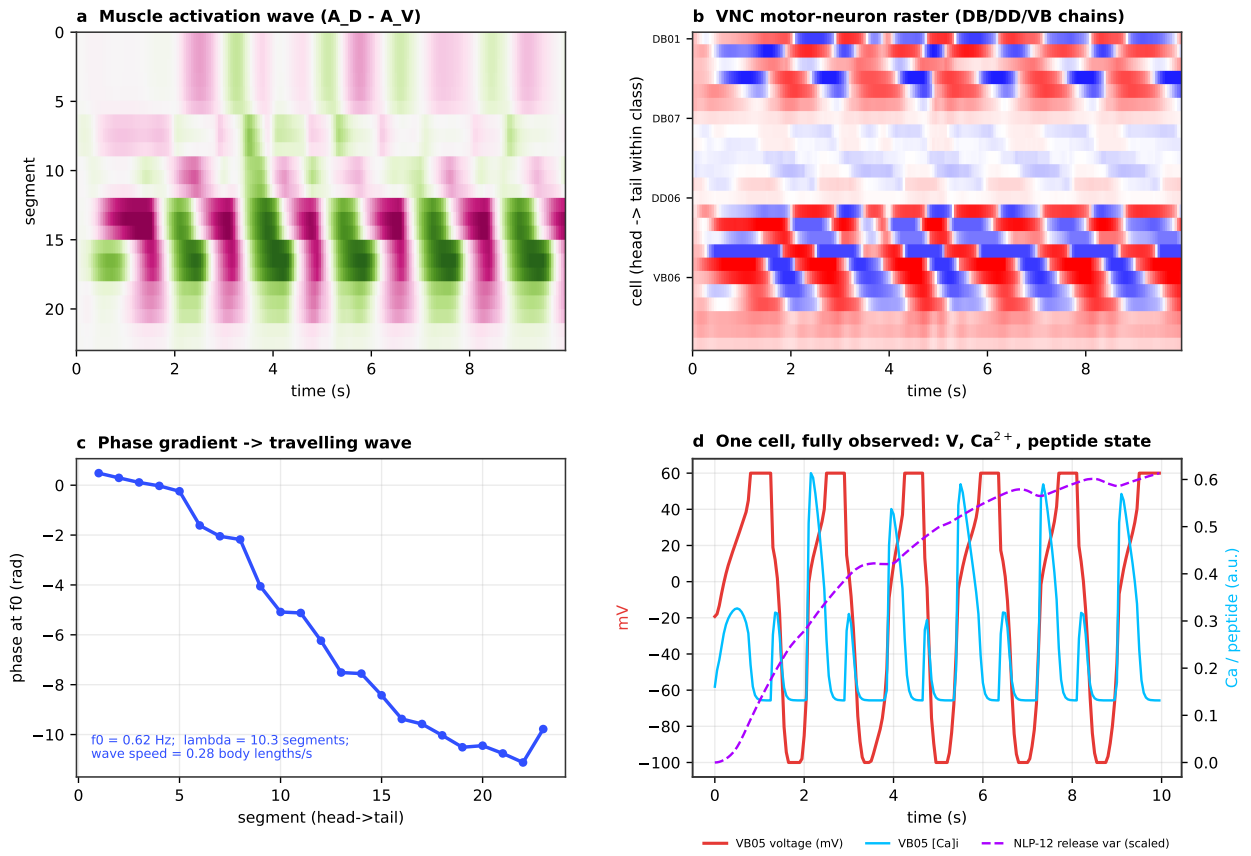


Figure 5. The locomotor wave is a stadium wave. a, Muscle-activation wave ($A_D - A_V$) along the body. **b,** Ventral-cord motor-neuron voltage raster (DB/DD/VB chains, head→tail within class): diagonal stripes are the activity wave running down the cord. **c,** Phase gradient at the dominant frequency: linear slope gives $\lambda = 10.3$ segments, $f_0 = 0.62$ Hz, wave speed ≈ 0.28 body lengths/s. **d,** Single-cell observability: VB05 voltage and intracellular Ca^{2+}, with the NLP-12 peptidergic variable overlaid.

strongest extrasynaptic functional edge in the whole-animal signal-propagation atlas [19] runs RIPL→AIML; the RIP neuron expresses its marker peptides *nlp-51* and *nlp-73* at four orders of magnitude above the expression threshold [69, 70], yet no receptor is recorded for either ligand in the system-wide deorphanization screen [16], and RIP itself is the neuron–pharynx link whose function has remained unexplored [70]. Sequence and expression intersection let us name candidates: *nlp-73* carries the twin-cysteine loop of calcitonin/DH31-like peptides, pointing to a class-B (secretin-like) GPCR — consistent with its absence from a screen built mainly on class-A NPR/FRPR receptors — and for *nlp-51* the orphan NPR-family receptors *f59d12.1* and *npr-23* each cover 9 of the 11 functional RIPL target cells (Table S4). Expression intersection is a necessity screen, not sufficiency; we state the prediction and its knock-out falsification test rather than fit a receptor into the model.

What this enables. Because the platform is modular and every constant is sourced, it functions as infrastructure: a new measurement enters as a module (as the muscle96 layer, the RIS terminator, and the unc-1 gap-junction state rule already have); a mutation or drug becomes a configuration change with a literature anchor (the *trp-4* phenocopy/rescue is the worked example); and disease-relevant channel or modulator variants can be screened against behaviour before any animal is touched — the logic validated in cardiac safety pharmacology [29], now operating at whole-animal scale.

4 Methods

4.1 Connectome and weights

The somatic connectome (323 cells) was assembled from Cook et al. [2] as updated by Witvliet et al. [3] with the public adjacency releases [4]. Chemical edge $j \to i$ carries weight $w_{ij} = g_{\mathrm{syn}}\, n_{ij}$ with n_{ij} the EM contact number and $g_{\mathrm{syn}} = 0.02$ (bounded, Table 5); sign from transmitter identity (ACh, Glu excitatory

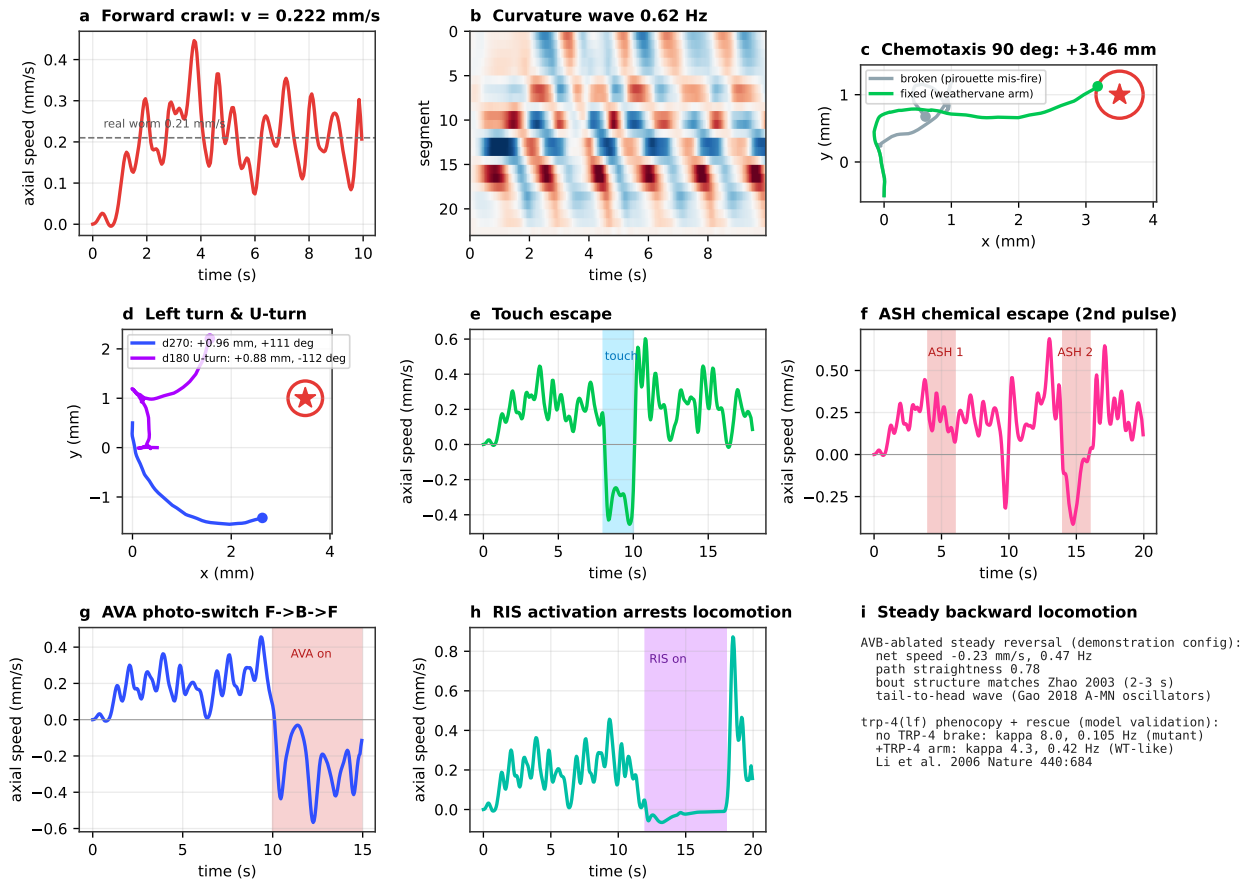


Figure 6. Seven-behaviour suite (frozen platform, real data from archived runs). a, Forward crawl axial speed (dashed: real-worm 0.21 mm s^{-1}). **b,** Crawl curvature kymograph. **c,** Chemotaxis, 90° assay: trajectory onto the source (+3.46 mm), shown against the mis-firing-pirouette control (Fig. 7). **d,** 270° (left-turn) and 180° (U-turn via pirouette) assays. **e,** Gentle-touch escape: reversal bout (shaded stimulus). **f,** ASH chemical escape: response on the second pulse (weak pass, see text). **g,** AVA photo-mimetic switch F→B→F. **h,** RIS activation arrests locomotion. **i,** Steady-backward configuration and the *trp-4* validation (Fig. 8).

$E^{\mathrm{rev}} = 0$ mV; GABA inhibitory, global E:I multiplier 5.0, declared estimate). Gap junctions are symmetric ohmic couplings proportional to contact number with the state-dependent gain of Eq. (2). Cell coverage by class: sensory 79, interneurons 80 (including the ten command cells of classes AVA, AVB, AVD, AVE and PVC), motor/head-motor 121, undetermined 3 (VAn, CANL, CANR), connectome muscle 32, glia 7 (three GLR + four CEP sheath), remnant 1 — total 323; per-cell classes in Supplementary Table S5.

4.2 Neuron model

Each cell integrates

$$C_m \dot{V}_i = -\sum_k I_{k,i} - I_i^{\mathrm{syn}} - I_i^{\mathrm{gap}} + I_i^{\mathrm{ext}}, \qquad I_k = g_k\, m^p h^q\, (V - E_k), \qquad \dot{x} = \frac{x_\infty(V) - x}{\tau_x(V)}, \tag{1}$$

with 17 currents and 29 state variables (voltage, 27 gates, intracellular Ca^{2+}) [35, 36]. Resting potentials per class are re-anchored to published recordings by bisection on the leak reversal [36, 32]; membrane voltage is numerically bounded to $[-80, +80]$ mV, a declared $\sim 3\times$ compression of the biological scale. Chemical transmission is graded with a piecewise-linear release table $r_j = \mathrm{clip}((V_j - v_j^{\mathrm{rel}})/25, 0, 1.5)$; gap junctions are ohmic,

$$I_i^{\mathrm{gap}} = \sum_j g_{\mathrm{eff},ij}\,(V_i - V_j), \qquad g_{\mathrm{eff},ij} = \big(1 - k(1 - M)\big)\, G_{\mathrm{gap}}\, w_{ij}, \tag{2}$$

with $k = 0.7$ from unc-1/innexin measurements [38] and M a slow state variable reporting anterior-sensory/dopaminergic tone. Command gating: the forward/backward motor programs are admitted by AVB/AVA depolarization with RIS veto and SMD/RIV steering biases [67, 20, 53, 55]. Three subcellular

Table 7. Behavioural validation summary. All runs on the frozen configuration; metrics from archived trajectories. References in Table 1 and text.

Assay	Model	Wet-lab reference
Forward crawl	0.222 mm s^{-1}, 0.62 Hz, $\kappa_{\text{amp}} =$ 4.03 mm^{-1}	0.21 mm s^{-1}, 0.58 Hz [6, 25]; band 3–5 mm^{-1} [7, 47]
Steady backward	-0.23 mm s^{-1}, 0.47 Hz, bouts 2–3 s	bout statistics [40]; A-MN oscillators [63]
Chemotaxis 90°/270°	+3.46 mm / +0.96 mm approach	weathervane mechanism [54]
U-turn 180°	$-111.7°$ via reversal-bout events	pirouette strategy [68]; omega amplitudes [47]
Touch escape	bout axial speed -0.230 mm s^{-1}	tap-withdrawal circuit [22, 39]
ASH escape	response on 2nd pulse (-0.185 mm s^{-1})	**weak pass**; ASH::ChR2 protocols [57]; modulation gap [52]
AVA switch	F→B→F within ±1 s	AVA activation drives reversal [22, 21, 20, 19]
RIS arrest	speed 0.17 → 0.01–0.05 mm s^{-1}, recovery on offset	RIS activation [23, 24, 20]
trp-4 phenocopy + rescue	κ 8.0 → 4.3 mm^{-1}, 0.105 → 0.42 Hz (steady-backward configuration)	exaggerated bending of *trp-4(lf)* [18]

mechanisms carry their literature forms: an AVA regenerative plateau (bistable, $\tau_2 = 0.5$ s [61, 32]); activity-dependent SLO-1/2 K^+ negative feedback downstream of UNC-2 (threshold 15 mV); and A-class motor-neuron local oscillators for the backward program [63, 64, 65]. RIS terminates reversal bouts as a transient brake (drive 14 pA, $\tau = 1.0/0.3$ s [20]) with a 4 s post-reversal refractory [39].

4.3 Muscle layer (96 cells)

Each muscle cell i receives NMJ drive $I_i = \sum_n s_n \, (w_{ni}^{\text{out}}/n_i^{\text{inn}}) \, r_n$ with $s_n = +1$ for cholinergic and -0.61 for GABAergic edges [43], and integrates

$$\tau_e \, \dot{m}_i^E = \text{clip}(I_i g, \, 0, \, A_{\max}) - m_i^E, \qquad \tau_{Ca} \, \dot{m}_i^A = \text{GJ}(m^E)_i - m_i^A, \tag{3}$$

with $\tau_e = 15.5$ ms [42, 41], $\tau_{Ca} = 300$ ms [7, 48], $A_{\max} = 1.5$, and GJ the steady-state innexin lattice solve with longitudinal coupling 0.25 [44]. Row activations $A_D[r] = \frac{1}{2}(m^A_{DR_r} + m^A_{DL_r})$ (and A_V likewise) set preferred curvature $\kappa_0[r] = \kappa_{\max}(A_D - A_V)$, $\kappa_{\max} = 16$ mm^{-1} [7, 47]. A tonic-release baseline is subtracted so that activation represents deviation from rest tension; motor-class direction gating (B/DD forward, A/VD backward) follows the command state [67, 20].

4.4 Body and proprioception

The body is a 24-segment viscoelastic rod in the preferred-curvature formulation [5, 6], equations of motion after Chung et al. [9], with bending elasticity $b = 4 \times 10^{-12}$ N m^3 [45]. Proprioception enters through (i) short-range B-chain coupling (drive -12 pA, offset -6 segments, delay $\tau_c = 80$ ms, field span $0.2L$, slope 0.62) [7] and (ii) the DVA/TRP-4 stretch arm [18]. Integration uses a fixed-step explicit scheme at $\Delta t = 0.025$ ms; a 20 s trial simulates in a few minutes on one CPU core.

4.5 Peptidergic axes

The DVA→NLP-12→CKR-2 axis follows

$$\tau_m \dot{m} = \min\big(\langle|\kappa|\rangle/\kappa_{\text{ref}}, \, 1\big) - m, \qquad g_{\text{NMJ}} = 1 + \alpha \, m, \tag{4}$$

with $\tau_m = 3$ s, $\kappa_{\text{ref}} = 3$ mm^{-1}, $\alpha = 0.25$ [17, 18]; the FLP-14→FRPR-19 arm provides reversal-bout positive feedback [58], gated by the AVA-state machinery [59, 60].

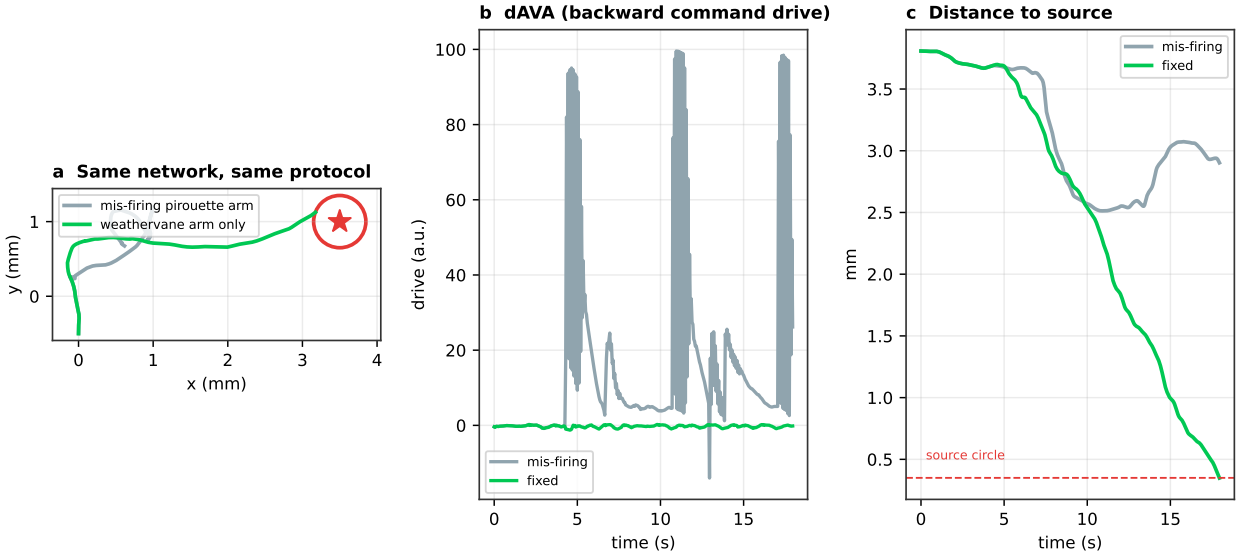


Figure 7. Mechanism-level debugging of chemotaxis. a, Same network, same 90° protocol: with the pirouette arm mis-firing (grey) the animal loops; with strategy gating correct (green) it curves onto the source (+3.46 mm). **b,** Backward-command drive (dAVA): illegitimate ignition events in the broken run, silent in the fixed run. **c,** Distance to source over time.

4.6 Sensory protocols

Salt chemotaxis: ASE reports dC/dt of a Gaussian source (σ = 2 mm); the weathervane arm maps it onto SMD/RIV head-steering curvature bias [54, 53, 55, 56, 51], and the pirouette arm fires reversal-bout re-orientation events for large heading errors [68]; the two arms are gated by strategy, never simultaneously. Gentle touch: ALM/PLM-class drive onto AVD/PVC with the tap-withdrawal polarity of Chalfie 1985 [22, 39]. ASH escape: two-pulse protocol after ASH::ChR2 experiments [57]. Photo-mimetic activation injects 50–400 pA into the named class during the stated windows (per-assay amplitudes in Supplementary Table S2) [21, 20, 23, 24].

4.7 Metrics

Speed: axial centre-of-mass velocity along the head–tail axis. Frequency: dominant FFT component of mid-body curvature (10 s analysis window after settling; FFT bin 0.125 Hz). Wave parameters: phase gradient of the curvature field at f_0 (Fig. 5c). Amplitude: mean absolute curvature peak. Chemotaxis: net approach to the source centre and net heading change. All metrics after a 1 s settling window; every figure number is computed from the archived trajectories shipped with the release.

4.8 Code and data availability

The sealed model (engine, connectome tables, constant ledger with per-row provenance, protocol blocks, figure scripts and archived runs) accompanies this paper as a self-contained release directory (`model_release_v3/`); every trajectory underlying every figure regenerates from the documented commands. The body layer used by every reported trajectory—the 24-segment viscoelastic rod with analytic-gradient forces (`engine/rod2d_own.py`) and the 96-cell body-wall muscle layer (`engine/muscle96.py`)—is original code implementing published equations [45, 5, 6, 9]. Legacy body modules derived from worm-whisperer (`https://github.com/kairess/worm-whisperer`) [10] remain in the release solely to reproduce archived early-development runs (`--rod2d borrowed` fallback) and are not exercised by any trajectory reported here; all other code is original.

Competing interests

The author declares no competing interests.

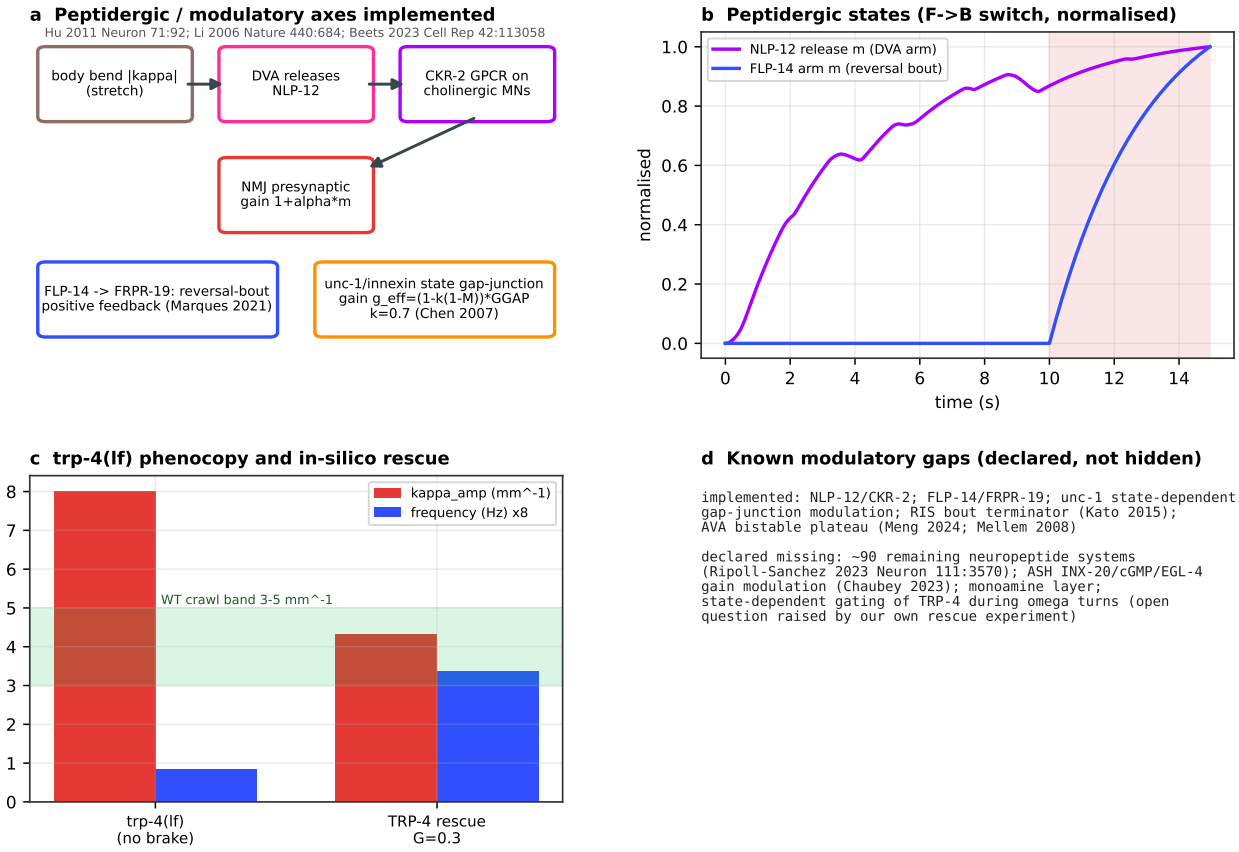


Figure 8. Modulatory layers implemented, and the *trp-4* validation. **a,** The three modulatory axes in the platform (mechanisms from [17, 18, 58, 38]). **b,** Peptidergic state variables during a forward→backward switch (shaded: backward command): NLP-12 arm active in crawling, FLP-14 arm recruited in the reversal phase. **c,** *trp-4(lf)* phenocopy and in-silico rescue: removing the TRP-4 stretch arm reproduces the mutant's exaggerated bending; reinstating it restores WT-band curvature [18]. **d,** Declared modulatory gaps (text).

Table 8. Whole-worm models at a glance.

Model	Neuron dynamics	Channel detail	Weights	Wave origin	Behaviour-level validation	Modulation
c302 / OpenWorm [11, 12]	Reduced single-compartment	Partial (K^+, Ca^{2+})	Fitted	Injected pacemaker current required	Qualitative locomotion	None
Kunert et al. 2014 [13]	Linear / minimal point neurons	None	Analytic + optimized	Bifurcation to limit cycle	Sensory-to-motor flow, modes	None
worm-whisperer [8, 10]	Distilled oscillator units	None	Trained to kinematics	Learned	Forward/reverse kinematics; chemotaxis under evolved stimulation [10]	None
BAAIWorm [14]	Multi-compartment (5 fitted, group-generalized)	14 fitted classes	Weights + polarities trained on calcium correlations	Trained network drives body	Zigzag foraging, structural lesions	None
This work	Conductance-based, 29 ODEs/cell, 323 cells	**17 currents/cell; anchored + re-derived constants**	**EM contact counts; none trained**	**Emergent: proprioceptive loop + command drive**	**7-assay suite vs. wet-lab refs; mutant phenocopy + rescue**	**Peptidergic axes + state-dependent gap junctions, simulated**

References

[1] White, J. G., Southgate, E., Thomson, J. N. & Brenner, S. The structure of the nervous system of the nematode *Caenorhabditis elegans*. *Phil. Trans. R. Soc. B* **314**, 1–340 (1986). doi:10.1098/rstb.1986.0056

[2] Cook, S. J. et al. Whole-animal connectomes of both *Caenorhabditis elegans* sexes. *Nature* **571**, 63–71 (2019). doi:10.1038/s41586-019-1352-7

[3] Witvliet, D. et al. Connectomes across development reveal principles of brain maturation. *Nature* **596**, 257–261 (2021). doi:10.1038/s41586-021-03778-8

[4] Varshney, L. R. et al. Structural properties of the *Caenorhabditis elegans* neuronal network. *PLoS Comput. Biol.* **7**, e1001066 (2011). doi:10.1371/journal.pcbi.1001066

[5] Boyle, J. H. & Cohen, N. *Caenorhabditis elegans* body wall muscles are simple actuators. *BioSystems* **94**, 170–181 (2008). doi:10.1016/j.biosystems.2008.05.025

[6] Boyle, J. H., Berri, S. & Cohen, N. Gait modulation in *C. elegans*: an integrated neuromechanical model. *Front. Comput. Neurosci.* **6**, 10 (2012). doi:10.3389/fncom.2012.00010

[7] Wen, Q. et al. Proprioceptive coupling within motor neurons drives *C. elegans* forward locomotion. *Neuron* **76**, 750–761 (2012). doi:10.1016/j.neuron.2012.08.039

[8] Chung, T. & Kim, S. Optimization of connectome weights for a neural network model generating both forward and backward locomotion in *C. elegans*. *Sci. Rep.* **16**, 21630 (2026). doi:10.1038/s41598-026-54384-5

[9] Chung, T., Chang, I. & Kim, S. Development of equation of motion deciphering locomotion including omega turns of *Caenorhabditis elegans*. *eLife* **12**, RP92562 (2024). doi:10.7554/eLife.92562

[10] Lee, T. What an atlas-fitted connectome can and cannot do: evolutionary search over interneuron stimulation in a whole-body *C. elegans* model. *bioRxiv* 2026.09.06.749731 (2026). doi:10.64898/2026.09.06.749731

[11] Gleeson, P. et al. c302: a multiscale framework for modelling the nervous system of *Caenorhabditis elegans*. *Phil. Trans. R. Soc. B* **373**, 20170379 (2018). doi:10.1098/rstb.2017.0379

[12] Szigeti, B. et al. OpenWorm: an open-science approach to modelling *Caenorhabditis elegans*. *Front. Comput. Neurosci.* **8**, 137 (2014). doi:10.3389/fncom.2014.00137

[13] Kunert, J., Shlizerman, E. & Kutz, J. N. Low-dimensional functionality of complex network dynamics. *Phys. Rev. E* **89**, 052805 (2014). doi:10.1103/PhysRevE.89.052805

[14] Zhao, M. et al. An integrative data-driven model simulating *C. elegans* brain, body and environment. *Nat. Comput. Sci.* **4**, 978–990 (2024). doi:10.1038/s43588-024-00738-w

[15] Ripoll-Sánchez, L. et al. The neuropeptidergic connectome of *C. elegans*. *Neuron* **111**, 3570–3589 (2023). doi:10.1016/j.neuron.2023.09.043

[16] Beets, I. et al. System-wide mapping of peptide–GPCR interactions in *C. elegans*. *Cell Rep.* **42**, 113058 (2023). doi:10.1016/j.celrep.2023.113058

[17] Hu, Z., Pym, E. C. G., Babu, K., Vashlishan Murray, A. B. & Kaplan, J. M. A neuropeptide-mediated stretch response links muscle contraction to changes in neurotransmitter release. *Neuron* **71**, 92–102 (2011). doi:10.1016/j.neuron.2011.04.021

[18] Li, W., Feng, Z., Sternberg, P. W. & Xu, X. Z. S. A *C. elegans* stretch receptor neuron revealed by a mechanosensitive TRP channel homologue. *Nature* **440**, 684–687 (2006). doi:10.1038/nature04538

[19] Randi, F., Sharma, A. K., Dvali, S. & Leifer, A. M. Neural signal propagation atlas of *Caenorhabditis elegans*. *Nature* **623**, 406–414 (2023). doi:10.1038/s41586-023-06683-4

[20] Kato, S. et al. Global brain dynamics embed the motor command sequence of *Caenorhabditis elegans*. *Cell* **163**, 656–669 (2015). doi:10.1016/j.cell.2015.09.034

[21] Piggott, B. J. et al. The neural circuits and synaptic mechanisms underlying motor initiation in *C. elegans*. *Cell* **147**, 922–933 (2011). doi:10.1016/j.cell.2011.08.053

[22] Chalfie, M. et al. The neural circuit for touch sensitivity in *Caenorhabditis elegans*. *J. Neurosci.* **5**, 956–964 (1985). doi:10.1523/JNEUROSCI.05-04-00956.1985

[23] Turek, M., Lewandrowski, I. & Bringmann, H. An AP2 transcription factor is required for a sleep-active neuron to induce sleep-like quiescence in *C. elegans*. *Curr. Biol.* **23**, 2215–2223 (2013). doi:10.1016/j.cub.2013.09.028

[24] Steuer Costa, W. et al. A GABAergic and peptidergic sleep neuron as a locomotion stop neuron with compartmentalized Ca^{2+} dynamics. *Nat. Commun.* **10**, 4095 (2019). doi:10.1038/s41467-019-12098-5

[25] Vidal-Gadea, A. et al. *Caenorhabditis elegans* selects distinct crawling and swimming gaits via dopamine and serotonin. *Proc. Natl. Acad. Sci. USA* **108**, 17504–17509 (2011). doi:10.1073/pnas.1108673108

[26] Prinz, A. A., Bucher, D. & Marder, E. Similar network activity from disparate circuit parameters. *Nat. Neurosci.* **7**, 1345–1352 (2004). doi:10.1038/nn1352

[27] Marder, E. & Goaillard, J.-M. Variability, compensation and homeostasis in neuron and network function. *Nat. Rev. Neurosci.* **7**, 563–574 (2006). doi:10.1038/nrn1949

[28] O'Leary, T. et al. Cell types, network homeostasis, and pathological compensation from a biologically plausible ion channel expression model. *Neuron* **82**, 809–821 (2014). doi:10.1016/j.neuron.2014.04.002

[29] Li, H. Data-extracted gating kinetics yield parameter-efficient, predictive models of four cardiac ion channels. *Research Square* (posted 1 October 2026). doi:10.21203/rs.3.rs-11218939/v1

[30] Jospin, M. et al. Characterization of K^+ currents using an in situ patch clamp technique in body wall muscle cells from *Caenorhabditis elegans*. *J. Physiol.* **544**, 373–384 (2002). doi:10.1113/jphysiol.2002.022293

[31] Jospin, M. et al. The L-type voltage-dependent Ca^{2+} channel EGL-19 controls body wall muscle function in *Caenorhabditis elegans*. *J. Cell Biol.* **159**, 337–348 (2002). doi:10.1083/jcb.200203055

[32] Mellem, J. E., Brockie, P. J., Madsen, D. M. & Maricq, A. V. Action potentials contribute to neuronal signaling in *C. elegans*. *Nat. Neurosci.* **11**, 865–867 (2008). doi:10.1038/nn.2131

[33] Richmond, J. E. & Jorgensen, E. M. One GABA and two acetylcholine receptors function at the *C. elegans* neuromuscular junction. *Nat. Neurosci.* **2**, 791–797 (1999). doi:10.1038/12160

[34] Goodman, M. B., Hall, D. H., Avery, L. & Lockery, S. R. Active currents regulate sensitivity and dynamic range in *C. elegans* neurons. *Neuron* **20**, 763–772 (1998). doi:10.1016/S0896-6273(00)81014-4

[35] Nicoletti, M. et al. Biophysical modeling of *C. elegans* neurons: single ion currents and whole-cell dynamics of AWC^{on} and RMD. *PLoS ONE* **14**(7), e0218738 (2019). doi:10.1371/journal.pone.0218738

[36] Nicoletti, M. et al. Biophysical modeling of the whole-cell dynamics of *C. elegans* motor and interneurons families. *PLoS ONE* **19**(3), e0298105 (2024). doi:10.1371/journal.pone.0298105

[37] Ranjan, R. et al. Channelpedia: an integrative and interactive database for ion channels. *Front. Neuroinform.* **5**, 36 (2011). doi:10.3389/fninf.2011.00036

[38] Chen, B. et al. UNC-1 regulates gap junctions important to locomotion in *C. elegans*. *Curr. Biol.* **17**, 1334–1339 (2007). doi:10.1016/j.cub.2007.06.060

[39] Wicks, S. R. & Rankin, C. H. Integration of mechanosensory stimuli in *Caenorhabditis elegans*. *J. Neurosci.* **15**, 2434–2444 (1995). doi:10.1523/JNEUROSCI.15-03-02434.1995

[40] Zhao, B., Khare, P., Feldman, L. & Dent, J. A. Reversal frequency in *Caenorhabditis elegans* represents an integrated response to natural stimuli. *J. Neurosci.* **23**, 5319–5328 (2003). doi:10.1523/JNEUROSCI.23-12-05319.2003

[41] Liu, P., Chen, B. & Wang, Z. W. Genetic dissection of ion currents underlying all-or-none action potentials in *C. elegans* body-wall muscle cells. *J. Physiol.* **589**, 101–117 (2011). doi:10.1113/jphysiol.2010.200683

[42] Gao, S. & Zhen, M. Action potentials drive body wall muscle contractions in *Caenorhabditis elegans*. *Proc. Natl. Acad. Sci. USA* **108**, 2557–2562 (2011). doi:10.1073/pnas.1012346108

[43] Liu, Q., Hollopeter, G. & Jorgensen, E. M. Graded synaptic transmission at the *Caenorhabditis elegans* neuromuscular junction. *Proc. Natl. Acad. Sci. USA* **106**, 10823–10828 (2009). doi:10.1073/pnas.0903570106

[44] Liu, Q., Chen, B., Hall, D. H. & Wang, Z. W. Gap junctions synchronize action potentials and Ca^{2+} transients in *Caenorhabditis elegans* body wall muscles. *J. Biol. Chem.* **286**, 44285–44293 (2011). doi:10.1074/jbc.M111.292078

[45] Fang-Yen, C. et al. Biomechanical analysis of gait adaptation in the nematode *Caenorhabditis elegans*. *Proc. Natl. Acad. Sci. USA* **107**, 20323–20328 (2010). doi:10.1073/pnas.1003016107

[46] Stephens, G. J., Johnson-Kerner, B., Bialek, W. & Ryu, W. S. Dimensionality and dynamics in the behavior of *C. elegans*. *PLoS Comput. Biol.* **4**, e1000028 (2008). doi:10.1371/journal.pcbi.1000028

[47] Broekmans, O. D., Rodgers, J. B., Ryu, W. S. & Stephens, G. J. Resolving coiled shapes reveals new reorientation behaviors in *C. elegans*. *eLife* **5**, e17227 (2016). doi:10.7554/eLife.17227

[48] Butler, V. J. et al. A consistent muscle activation strategy underlies crawling and swimming in *Caenorhabditis elegans*. *J. R. Soc. Interface* **12**, 20140963 (2015). doi:10.1098/rsif.2014.0963

[49] Pierce, S. et al. Neuromechanical phase lags and gait adaptation in the nematode *C. elegans*. *PRX Life* **3**, 023001 (2025). doi:10.1103/PRXLife.3.023001

[50] Narayan, A., Laurent, G. & Sternberg, P. W. Transfer characteristics of a thermosensory synapse in *Caenorhabditis elegans*. *Proc. Natl. Acad. Sci. USA* **108**, 9667–9672 (2011). doi:10.1073/pnas.1106617108

[51] Tolstenkov, O. O. et al. Functionally asymmetric motor neurons contribute to coordinating locomotion of *C. elegans*. *eLife* **7**, e34997 (2018). doi:10.7554/eLife.34997

[52] Chaubey, A. et al. The *Caenorhabditis elegans* innexin INX-20 regulates nociceptive behavioral plasticity. *Genetics* **223**, iyad017 (2023). doi:10.1093/genetics/iyad017

[53] Gray, J. M., Hill, J. J. & Bargmann, C. I. A circuit for navigation in *Caenorhabditis elegans*. *Proc. Natl. Acad. Sci. USA* **102**, 3184–3191 (2005). doi:10.1073/pnas.0409009101

[54] Iino, Y. & Yoshida, K. Parallel use of two behavioral mechanisms for chemotaxis in *C. elegans*. *J. Neurosci.* **29**, 5370–5380 (2009). doi:10.1523/JNEUROSCI.3633-08.2009

[55] Hendricks, M., Ha, H., Maffey, N. & Zhang, Y. Compartmentalized calcium dynamics in a *C. elegans* interneuron encode head movement. *Nature* **487**, 99–103 (2012). doi:10.1038/nature11081

[56] Kramer, A. et al. Neural sequences underlying directed turning in *C. elegans*. *Nat. Neurosci.* **29**, 1408–1424 (2026). doi:10.1038/s41593-026-02257-5

[57] Guo, Z. V., Hart, A. C. & Ramanathan, S. Optical interrogation of neural circuits in *Caenorhabditis elegans*. *Nat. Methods* **6**, 891–896 (2009). doi:10.1038/nmeth.1397

[58] Marques, F. C. et al. Signaling via the FLP-14/FRPR-19 neuropeptide pathway sustains nociceptive responses in *C. elegans*. *PLoS Genet.* **17**, e1009880 (2021). doi:10.1371/journal.pgen.1009880

[59] Sordillo, A. & Bargmann, C. I. Behavioral control by depolarized and hyperpolarized states of an integrating neuron. *eLife* **10**, e67723 (2021). doi:10.7554/eLife.67723

[60] Katz, M. et al. Glutamate spillover in *C. elegans* triggers repetitive behavior through presynaptic glutamate receptor MGL-2/mGluR5. *Nat. Commun.* **10**, 1882 (2019). doi:10.1038/s41467-019-09581-4

[61] Meng, J. et al. A tonically active master neuron modulates mutually exclusive motor states at two timescales. *Sci. Adv.* **10**, eadk0002 (2024). doi:10.1126/sciadv.adk0002

[62] Xu, T. et al. Descending pathway facilitates undulatory wave propagation in *Caenorhabditis elegans* through gap junctions. *Proc. Natl. Acad. Sci. USA* **115**, E4493–E4502 (2018). doi:10.1073/pnas.1717022115

[63] Gao, S. et al. Excitatory motor neurons are local oscillators for backward locomotion. *eLife* **7**, e29915 (2018). doi:10.7554/eLife.29915

[64] Fouad, A. D. et al. Distributed rhythm generators underlie *Caenorhabditis elegans* forward locomotion. *eLife* **7**, e29913 (2018). doi:10.7554/eLife.29913

[65] Olivares, E. et al. Potential role of a ventral nerve cord central pattern generator in forward and backward locomotion in *Caenorhabditis elegans*. *Netw. Neurosci.* **2**, 323–343 (2018). doi:10.1162/netn_a_00036

[66] Ji, N. et al. Phase response analyses support a relaxation oscillator model of locomotor rhythm generation in *Caenorhabditis elegans*. *eLife* **10**, e69905 (2021). doi:10.7554/eLife.69905

[67] Kawano, T. et al. An imbalancing act: gap junctions reduce the backward motor circuit activity to bias *C. elegans* forward locomotion. *Neuron* **72**, 572–586 (2011). doi:10.1016/j.neuron.2011.09.005

[68] Pierce-Shimomura, J. T., Morse, T. M. & Lockery, S. R. The fundamental role of pirouettes in *Caenorhabditis elegans* chemotaxis. *J. Neurosci.* **19**, 9557–9569 (1999). doi:10.1523/JNEUROSCI.19-21-09557.1999

[69] Taylor, S. R. et al. Molecular topography of an entire nervous system. *Cell* **184**, 4329–4347.e23 (2021). doi:10.1016/j.cell.2021.06.023

[70] Reilly, M. B. et al. Widespread employment of conserved *C. elegans* homeobox genes in neuronal identity specification. *PLoS Genet.* **18**, e1010372 (2022). doi:10.1371/journal.pgen.1010372

Supplementary Files

This is a list of supplementary files associated with this preprint. Click to download.

- wholewormplatformpreprintv3SI.pdf
- suiteS1forwardcrawl.mp4
- suiteS2chemotaxisd090.mp4
- suiteS3chemotaxisd270.mp4
- suiteS4chemotaxisd180.mp4
- suiteS5touchescape.mp4
- suiteS6ashescape.mp4
- suiteS7avaswitch.mp4
- suiteS8risarrest.mp4
- suiteS9crawloscilloscope.mp4
- suiteS10switchpeptidergic.mp4